RSC Advances

PAPER

View Article Online
View Journal | View Issue

Cite this: *RSC Adv.*, 2019, **9**, 26503

Fluorescent delivery vehicle containing cobalt oxide–umbelliferone nanoconjugate: DNA/protein interaction studies and anticancer activity on MF7 cancer cell line†

Mohd Sajid Ali,[a] Sartaj Tabassum,*[ac] Hamad A. Al-Lohedan,[a] Mohammad Abul Farah,[b] Khalid Mashay Al-Anazi[b] and Mohammad Usman[c]

Fluorescent labeling is limited to certain molecules and alters biomolecule functionality. A new class of nanomaterial with anticancer activity and fluorescence properties has been designed and prepared. This nanotherapeutic conjugate of natural molecules has a selective binding site in cancer cell lines. Natural drug umbelliferone was taken with cobalt metal ions in a one pot assembly in the presence of tannic acid which yields new fluorescent nanoparticles of umbelliferone cobalt oxide nanoconjugate. Umbelliferone has high fluorescent properties and also has coordination ability to bind with central metal ions. The nanoconjugate was synthesized and characterized by using TEM, EDX analysis, SEM, XRD, and FTIR spectroscopy. TEM shows that the average size of the particles formed with umbelliferone is ~20 nm. The solubility of the drug nanoparticles in water showed compatibility with cancer cells and provided a favorable environment to investigate the mechanism of action on the MCF-7 cell line. The nanoconjugate is microcrystalline in nature and gives a clear suspension in water. The nanocobalt conjugate was loaded on TiO_2 nanoparticles by ultrasonication, and the solution was digested overnight. The conjugate of the drug with a TiO_2 drug carrier was stable in solution and maintained the nanostructure ~34.6 nm. A comparative study with nano-vehicle TiO_2 and the nanoconjugate was performed. TiO_2 was used to compare the anti-cancer activity of the nanoconjugate at low dose *in vitro*. It was observed that the nanoconjugate with TiO_2 is capable of reaching the specific target like the TiO_2 nanoparticle and enhance the chemotherapeutic impact. Hence, the nanoconjugate can also be used like nano-TiO_2, as the drug and carrier. The ct-DNA and HSA protein binding studies were done and validated by docking studies.

Received 31st March 2019
Accepted 27th June 2019

DOI: 10.1039/c9ra02412c

rsc.li/rsc-advances

1. Introduction

Nanoparticle based conjugate biomaterials have opened a new area of research in medical sciences and radio-oncology. The nano-dimension molecules are being exploited for radio-diagnosis, chemotherapeutic, and enzyme mimicking applications.[1–3] Metal nanoparticles with paramagnetic properties are attractive because their optical, magnetic and chemical properties can be modified for biosensing.[4–6] Antibodies in life science have gained momentum, with their conjugates being used for targeted drug therapy.

The demand for labeling technologies has enabled the production of nanoconjugates for imaging and drug delivery properties. There is a need to develop dual functional nano-therapeutic bioconjugates for *in vivo* and *in vitro* model systems. Nano fluorescent molecules are important drugs for the diagnosis and treatment of cancer.[7,8]

The literature showed that the high concentrations of nano-TiO_2 induce lung cancer in mice.[9,10] TiO_2 nanoparticles can serve as potential tumor cell-killing agents, and gene targeting materials. The impacts of TiO_2 on cytotoxicity in renal and neural cells and ROS have thoroughly been investigated.[11]

Umbelliferone is a coumarin derivative and has anticoagulant[12,13] and fluorescent properties.[14] Transition metal complexes of umbelliferone derivatives synthesized, characterized and their antitumor activity has also been reported.[15–17] The Umbelliferae derivatives have high antimutagenic and anti-carcinogenic activity.[18]

[a]*Surfactant Research Chair, Department of Chemistry, College of Sciences, King Saud University, P.O. Box 2455, Riyadh 11451, Kingdom of Saudi Arabia. E-mail: tsartaj62@yahoo.com; Tel: +96 6530128012*

[b]*Department of Zoology, College of Sciences, King Saud University, Riyadh 11451, Kingdom of Saudi Arabia*

[c]*Department of Chemistry, Aligarh Muslim University, Aligarh-2002, India. Tel: +91 9358255791*

† Electronic supplementary information (ESI) available. See DOI: 10.1039/c9ra02412c

It has been reported that TiO_2 can move in the blood through plasma proteins, the specific interactions between nanoparticles and proteins are not well studied. The TiO_2 particles may react with cell membrane proteins, and interaction with DNA followed by ROS has an essential role in DNA damage, destruction of the membrane and finally cell death.[19]

The literature survey shows that a comparative study on nanoconjugate with TiO_2 nanoparticles is still in demand. That motivated us to synthesized fluorescent nano cobalt oxide conjugate, to explore its anti-cancer activity, and its prospective application in diagnostic medicine. A modified method was opted to get nano-complex of cobalt(II) with umbelliferone in the presence of tannic acid in the alkaline medium. Tannic acid, contains glucose and poly galloyl ester chains, hydrolyzes in both acidic and basic conditions and gives gallic acid and glucose. The fragments have weak reducing properties which protect high oxidation of cobalt ion. The umbelliferone is a coordination ligand and captures the cobalt oxide at room temperature and yields fluorescent nanoconjugate. *In vitro* biological evaluation suggests that no apparent toxicity of the TiO_2/CoO–umbelliferone coating and the conjugation stimulates the cell proliferation. Comparative study with TiO_2 and TiO_2–CoO–umbelliferone conjugate exhibits improved anti-cancer activity of the latter.

The surface modification of TiO_2 materials may provide hybrid material for the further development of bioactive duel function conjugate to better meet the medical demand. The literature survey shows that naturally occurring coumarins exhibit antimutagenic activity and prevent dimethyl benz(*a*) anthracene-induced mammary neoplasia.[19] Polymeric nanoparticles are widely used in pharmaceutical research. The objective of this project was to develop a new and economically viable nanoconjugate which has anti-cancer activity and fluorescence property as well. Here, we report a simple method to synthesize nano dual function fluorescent pharmaceuticals & probe and delivery agent like nano-TiO_2.

2. Material and methods

Umbelliferone, cobalt(II) nitrate hexahydrate obtained from Fluka Trypan blue, phosphate buffered saline (PBS), dimethyl sulfoxide (DMSO), ethidium bromide, acridine orange, and Dulbecco's Modified Eagle's medium (DMEM), Tannic acid and nano-TiO_2 obtained from Sigma-Aldrich (St Louis, MO, USA). CellTiter 96® Non-radioactive cell proliferation assay kit obtained from Promega (Madison, WI, USA). All reagents were of the best commercial grade and used without further purification. Fourier-transform IR (FTIR) spectra recorded on an Interspec 2020 FTIR spectrometer PerkinElmer Model 1320 spectrometer (KBr disk, 400–4000 cm^{-1}), PerkinElmer UV-vis spectrophotometer, Shimadzu RF-5301 PC spectrofluorophotometer. Axygen horizontal electrophoretic assembly with power supply and Vilber-Infinity gel documentation system for imaging. Powder X-ray diffraction (XRD) of the products was measured using a Philips X'Pert PRO MPD diffractometer at a scanning rate of 4° min^{-1}, with 2α ranging from 10° to 70°, using Cu Kα radiation (=1.5406 Å). Thermal studies were conducted using a TGA/SDTA 851e (Mettler Toledo) thermogravimetric analyzer in ambient atmosphere from 20 °C to 500 °C at a heating rate of 10 °C min^{-1}. The morphologies of the samples studied by scanning electron microscopy (SEM) (JEOL SM5600LV) at 20 kV. The powders were ultrasonicated in ethanol, and a drop of the suspension dried on a carbon-coated microgrid. Transmission electron microscopy (TEM) observations performed with a JEM 100CX-II microscope operated at 100 kV.

2.1. Synthesis of nanoconjugate

The synthesis of the nanoconjugate is done according to the simple procedure (Scheme 1) by using tannic acid as reducing and activating agent. A methanolic solution of cobalt nitrate (0.001 mol) was taken in a round bottom flask and umbelliferone was added (0.001 mol) to it to form a clear pink solution. To the stirring solution, tannic acid was added dropwise in open assembly. The solution of the reactants sonicated for one hour till a brown colored fine powder obtained. The product was centrifuged and washed with ethanol and again centrifuged and washed several times with ethanol and dried *in vaccuo*.

2.2. DNA binding and cleavage

DNA binding experiments were done using the standard protocol.[20] The MCF-7 human breast adenocarcinoma cell line was obtained from American Type Culture Collection (ATCC, Rockville, MD, USA) and cell were grown in DMEM with 10% FBS and 1% antibiotics at 37 °C with 5% CO_2 (for detail see ESI†). MTT colorimetric assay with some modifications was performed using a CellTiter 96® non-radioactive cell proliferations assay kit (Promega, Madison, WI, USA). Morphological changes in cells (MCF-7) after treatment with nanoconjugate for 24 h were visualized under 100× a phase contrast inverted microscope. Intracellular ROS generation was analysed by staining the cells after treatment with fluorescent dye (carboxy-H_2 DCFDA). Quantitative estimation of ROS was achieved by measuring fluorescence and qualitative observation was performed by acquiring images under fluorescence microscope. Acidic vesicular organelles (AVOs), as a marker of autophagy induction were observed by fluorescence microscopy after staining of cells with acridine orange (AO). An apoptosis DNA ladder kit (Roche Diagnostics, Mannheim, Germany) was used to analyse DNA fragmentation on agarose gel electrophoresis. All experiments were carried out with three independent replicates. Values were presented as mean ± standard error of the mean (SEM). Data were analyzed using the Student's *t*-test for comparison between the means applying a significance level of $P < 0.05$. For more details on these experiments see ESI.†

2.3. Molecular docking

The rigid molecular docking studies performed by using HEX 8.0.0 software, which is an interactive molecular graphics program for calculating and displaying available docking modes of protein. The Hex 8.0.0 performs protein docking using Spherical Polar Fourier Correlations[21] the parameters

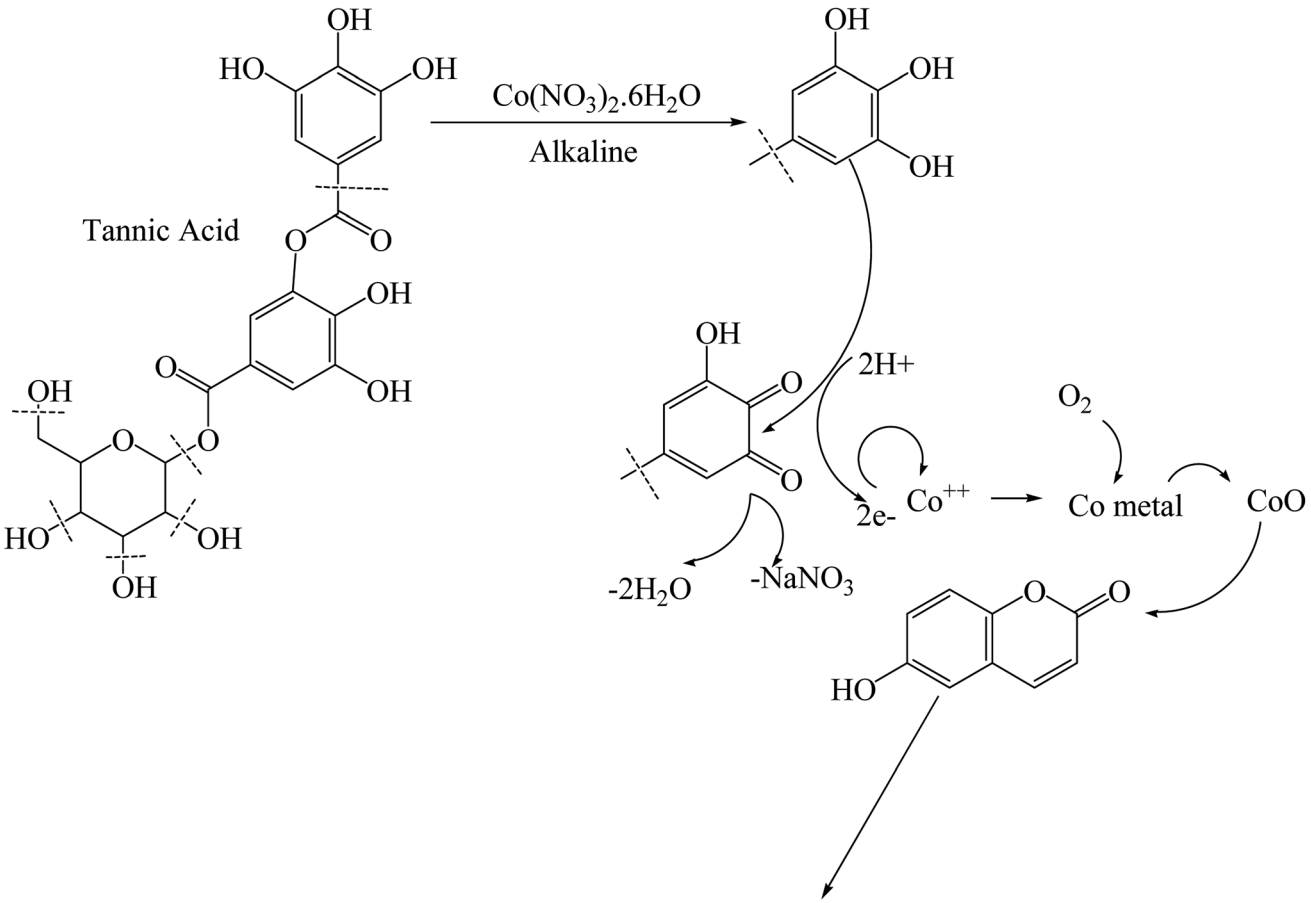

Scheme 1

used for docking include correlation type – shape only, FFT mode – 3D, grid dimension – 0.6, receptor range – 180, ligand range – 180, twist range – 360, distance range – 40. The crystal structure of DNA and the human serum albumin (PDB ID: 1bna, 1h9z) downloaded from the protein data bank (http://www.rcsb.org./pdb). Visualization of minimum energy favorable docked poses has been performed using Discovery studio 4.1.[22]

2.4. Binding of nanoconjugate with calf thymus DNA and HAS

HSA and DNA binding studies were carried out using UV-visible, fluorescence quenching and circular dichroism methods and the detailed experimental procedures for these studies have been described elsewhere.[20,23–27]

3. Result and discussion

Nanoconjugate has dual character as drug and a carrier, nanostructural arrangement enhance cellular uptake.[28–30] Immunomodulation of the drug has opened new sub-area of research.[31] Several self-assembled nanostructures have been studied by TEM and it has been observed that the driving forces such as hydrogen bonds and van der Waals forces exist. The effective delivery also depends on other factors, specific targeting, cell uptake, kinetics, and clearance. The present study was focused on nanoconjugation to minimize drug degradation and increase absorption in the cell. Natural organic conjugate nanoparticles possess many desirable features for drug delivery in three distinct interfaces, suitable for endocytosis, less toxic and biodegradable. To recognize and respond to biomolecules has recently been exploited to deliver therapeutic compounds *via* drug carrier. The loading mechanisms, therapeutic targets delivery, and efficacy enhanced many folds through this method. The importance of such nanoconjugate for drug/drug delivery agent, it has spaced structures for adsorbing second drug moiety. The cytotoxicity of this nanoconjugate evaluated on the receptor in the cell. Umbelliferone was successfully attached to the nanocobalt oxide nanoparticles by covalent interaction, exhibit cytotoxicity and induce apoptosis in cancer cells. Fluorescence microscopy study shows the dose of the conjugate particle absorbed by MF7 cancer cells, which demonstrated that cells overexpressing the conjugate receptor internalized a higher level of this nanoconjugate then TiO_2.

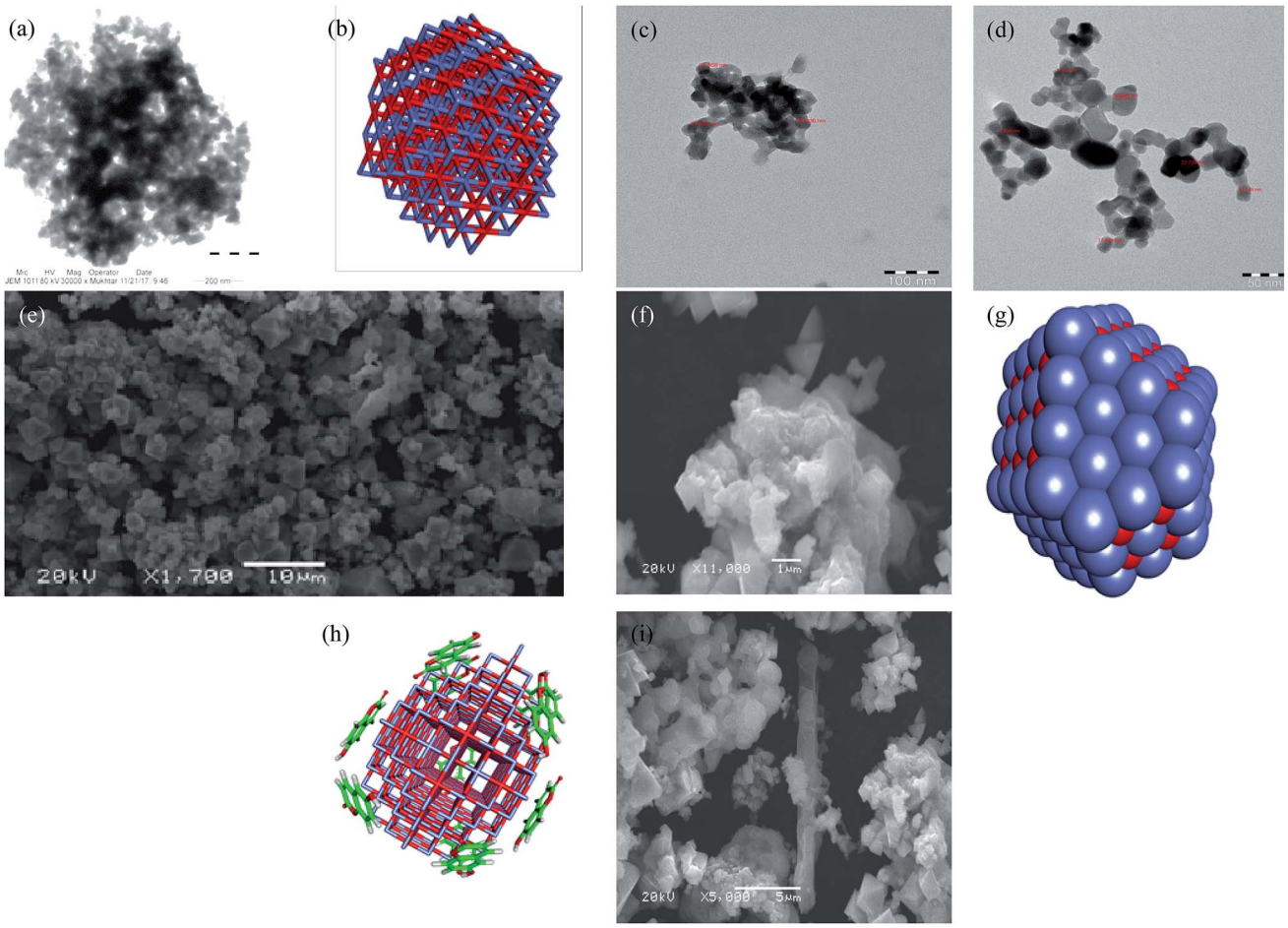

Fig. 1 TEM, SEM images inner and outer core of nanoconjugate (a–g); TEM (a, c and d) and SEM (e, f and i) images & computer generated model images of nanoconjugate (b, g, and h) of cobalt oxide nanoconjugate of umbelliferone.

3.1. Characterization of nanoconjugate

3.1.1. X-ray diffraction analysis. The XRD pattern of nanoconjugate was compared and interpreted with standard data of JCPDS file. The XRD pattern of cobalt oxide nanoparticles represented in Fig. 1. The characteristic peaks at 2θ 0 37.39°, 43.62°, 63.91° and 76.98° for cobalt oxide umbelliferone nanoconjugate (Fig. S1,† XRD) correspond to (220), (400), (511) and (440) respectively.[32] The XRD pattern indicates that particles are square pyramidal/cubic shape crystals which are further supported by SEM images, the particles size measured by TEM image, the average size of the complex was estimated to be 23 nm after calibrating the scale on the TEM and further calculated by Scherrer equation eqn (1)[33] the prominent peaks suggest successful conjugation of umbelliferone with CoO. A limited number of peaks in XRD indicate that there is no fragment of coordination complex of cobalt(II) ligand.

$$d = 0.9\lambda/\beta \cos\theta, \quad (1)$$

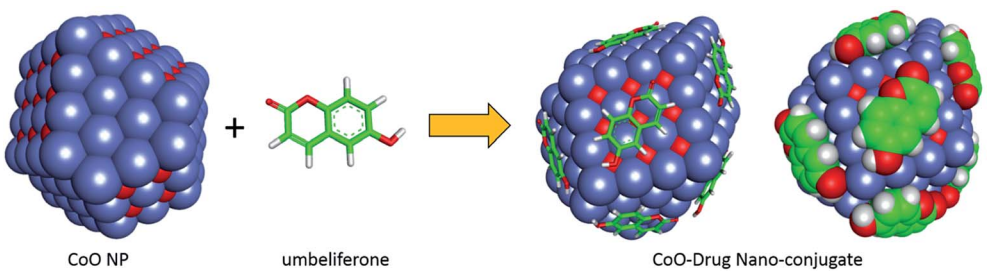

Fig. 2 Model presentation of the simulation of nanoconjugate.

where λ is the X-ray wavelength (0.154 nm, Cu Kα source); β is the Bragg's diffraction angle; θ is the FWHM of the peak.

3.1.2. FT IR spectroscopy. FTIR spectra show basic IR band characteristics of CoO at √M–O 566 cm^{-1}, which indicate the presence of CoO vibration and broadband around 3412 cm^{-1}, indicative of the presence of √OH groups on the nanoparticle surface. After conjugation, the spectrum shows the characteristic band of the CoO and umbelliferone in the nano-inner core and ligand oxygen donor atom (Fig. S2†). In addition to this, a band at 2930 cm^{-1} along with the √C=O stretching at 1612 cm^{-1} indicated that CoO conjugated to C=O and C–OH of umbelliferone. 763 cm^{-1},1069 cm^{-1} and 1231 cm^{-1}, 1372 cm^{-1} are due to C–O and C–O–C. The peak at 2840 cm^{-1} is due to C–H stretching vibration of umbelliferone.

3.1.3. TGA and mass spectrometry. The molecular mass and thermogravimetric analysis support the combination of nanoconjugate in [–Co=O···H–O–umbelliferone–C=O → Co=]O, the calculated mass $M/Z = 295.99$ (Fig. S3†) is close to the experimental value of nanoconjugate, *i.e.*, 293.199. The mass fragments 74 111 163 are the umbelliferone components as reported in the literature.[34,35] The TGA further support that the conjugate is non-hygroscopic nature, there is no remarkable loss below 100 °C. The organic moiety of umbelliferone resists fragmentation up to about 500 °C. The total loss in weight percentage supporting the loss of umbelliferone (Fig. S4†).

3.1.4. TEM and SEM imaging. Drug conjugation is the process by which component metal and ligand bond together to form a new drug formulation. The binding of the ligand and nanoparticle yielded single spherical nanoconjugates during the modified synthesis at room temperature.[36,37] The cobalt ion gets reduced in the presence of tannic acid and forms nanoconjugate. The single crystalline nature is confirmed by HRTEM and SEM images (Fig. 1) which shows that the well-defined arrangement in the structure. The SEM and TEM images simulated by computer-generated structures to understand packing pattern of Co–O and conjugation of umbelliferone. The corresponding transform pattern (Fig. 1e and g) of the HRSEM image also verifies that this single crystalline nanorod grows along the [001] direction. In the syntheses, the TEM image (Fig. 1a, c and d) of the products synthesized at room temperature shows a crystalline square/cubic pyramidal morphology with an average size 23 nm. Few of the nanorods split into two or more sub rods formed after an extended period of exposure to the air at room temperature.

3.1.5. Stability of nano-conjugate in water and in buffered saline system. Stability of nano-conjugate in water and in medical grade saline system was also seen and it was found that it was degraded 10% in water and 16% in medical grade saline system in 24 h. UV-visible spectra of nanoconjugate in water and in medical grade saline at physiological pH are given in Fig. S5a and b.† In future, a study can be designed to enhance the stability of this nano-conjugate which have various promising properties which will be discussed in the following parts of the manuscript.

3.2. Molecular docking

The literature on the docking or molecular simulation studies of the nano-drug conjugate is scarce. The main problem resides in the simulation of structural coordinates or molecular assembly of the nano-drug conjugate. Here we adopt a three-step molecular simulation protocol, (1) generation of 2 nm CoO nanoparticle atomic coordinates. (2) Interaction of nanoparticle with corresponding drug moiety to find out the surface level interaction and confirmation of drug moiety. (3) The molecular docking of

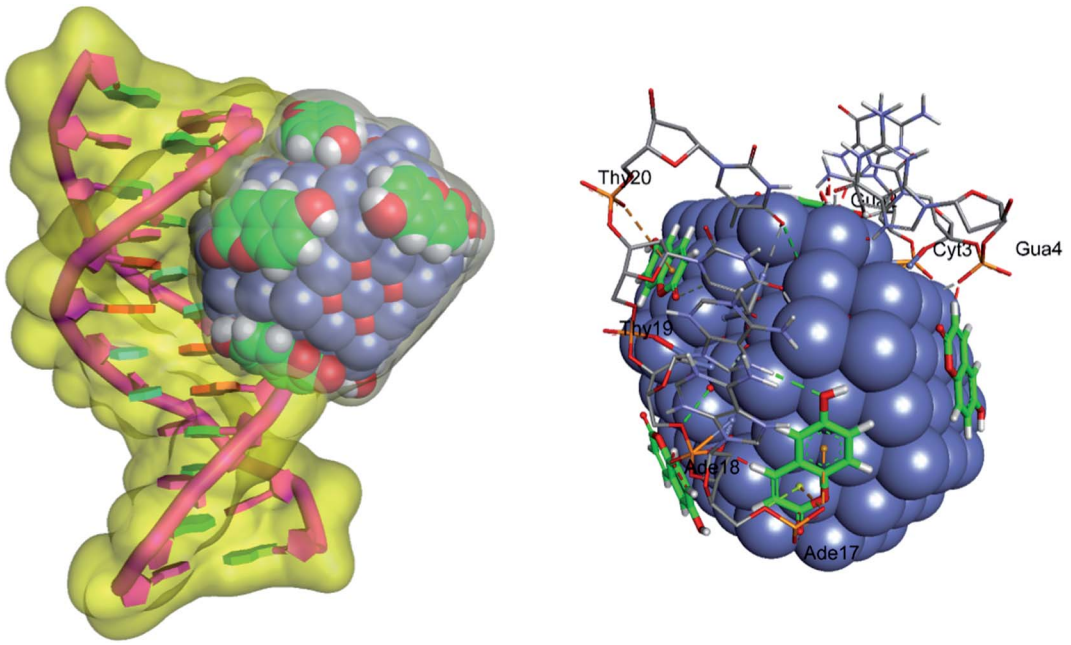

Fig. 3 Energy minimized most favorable molecular dock model of drug-nanoconjugate with DNA and binding site interactions.

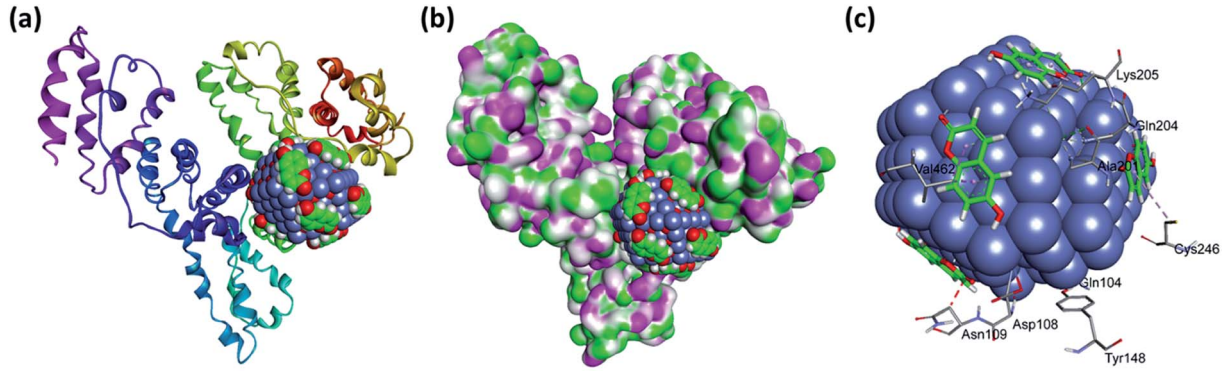

Fig. 4 (a) Molecular docked model of drug nanoconjugate (CPK) located within the hydrophobic pocket in subdomain IIA of HSA. (b) Molecular docked model with hydrogen bond donor–acceptor protein surface. (c) Molecular docked model of binding site interactions with pocket residues of the binding site I located in subdomain IIA of HSA.

drug nanoconjugate with DNA. The molecular assembly of 2 nm CoO generated from the crystal structure investigation file is directly taken from the CCDC. The generated 2 nm CoO nanoparticle molecular structure is then subjected to energy minimization along with the ten numbers of drug molecules by employing the molecular mechanic's force field.

3.2.1. Molecular docking with DNA. The nanodrug conjugate binding with DNA has attracted attention in the medicinal design of anticancer drugs. The docking studies are carried out to gain a deeper understanding of DNA interaction *in silico* for the prepared drug nanoconjugate. The confirmation of docked drug nanoconjugate is usually assessed for the kinds of non-covalent interaction between the DNA and nanoconjugate. The energetically favorable docked pose attained from the molecular docking of the nanoconjugate with a DNA duplex of sequenced $(CGCGAATTCGCG)_2$ dodecamer (PDB ID: 1BNA) was executed in order to predict the binding mode along with the most minimum energy favored orientation (Fig. 2 and 3). The result shows that nanoconjugate interacts by way of the major groove of DNA *via* hydrogen bonding, electrostatic and hydrophobic interactions as illustrated in Table S1.†[38]

3.2.2. Molecular docking with HSA. Molecular docking simulation was employed to find out the exact binding sites within the molecular target HSA. The reported 3-D structure of crystalline albumin HSA comprises of three homologous domains (denoted I, II, and III): I (residues 1–195), II (196–383) and III (384–585) that assemble to form a heart-shaped molecule. The key region of the nanoconjugate binding sites of HSA is located in hydrophobic cavities in subdomains IIA corresponding to sites I, and the tryptophan residue (Trp-214) of HSA in subdomain IIA. There is a large hydrophobic cavity in subdomain IIA (a binding site I) to accommodate drug nanoconjugate. The minimum energy docked pattern (Fig. 4a and b) indicates that drug nanoconjugate located within the subdomain IIA of HSA, forming numerous hydrophobic contacts (Pi-Sigma, Pi-Alkyl) with VAL462, CYS246, and LYS205, residues of hydrophobic binding site IIA (Fig. 4c). Furthermore, there are also some hydrogen bonds and specific metal acceptor interactions formed by the drug nanoconjugate (Table 1).

These non-covalent interaction formed by drug nanoconjugate dominated by hydrophobic contact while additional stabilization also assisted by the hydrogen bonding and other metal acceptor type noncovalent interactions with the polar residues of the binding site cavity. It was previously observed that hydrogen bonding and metal acceptor interaction

Table 1 Non-covalent interaction of drug nanoconjugate with HSA[a]

Name	Distance (Å)	Category	Type
:UNK1:O1 – A:ALA201:O	3.0465	Hydrogen bond	Hydrogen bond
A:LYS205:CA – :UNK1:O	3.45698	Hydrogen bond	C–H bond
A:LYS205:CE – :UNK1:O1	3.26261	Hydrogen bond	C–H bond
*A:LYS205:CE – :UNK1:O1	3.09276	Hydrogen bond	C–H bond
:UNK1:CO1 – A:TYR148:OH	3.03676	Other	Metal-acceptor
:UNK1:CO1 – A:GLN104:O	3.37952	Other	Metal-acceptor
A:VAL462:CG2 – :UNK1	2.45914	Hydrophobic	Pi–σ
A:VAL462:CG2 – :UNK1	3.29989	Hydrophobic	Pi–σ
:UNK1 – A:CYS246	5.44805	Hydrophobic	Pi-alkyl
:UNK1 – A:LYS205	4.07321	Hydrophobic	Pi-alky
:UNK1 – A:LYS205	4.22508	Hydrophobic	Pi-alkyl

[a] Note: UNK1 = nanodrug-conjugate.

decreased the hydrophilicity and increased the hydrophobicity to keep the drug nanoconjugate – HSA system stable.[39]

3.3. *In vitro* DNA and HSA binding studies in solutions

UV-visible spectroscopy was employed to see the changes in the UV-visible spectral profiles of ct-DNA in the presence of nanoconjugate (Fig. 5). Hyperchromism was observed with increasing concentration of ct-DNA confirming the interaction of complex and ct-DNA which suggests the possibility of interactions between them. The apparent rate constant was evaluated using Benesi–Hildebrand equation[40] which was found to be 1.67×10^4 M^{-1}. For getting more insight on the interaction between ct-DNA and nanoconjugate dye displacement method (using EB and DAPI) along with circular dichroism spectroscopy performed, and the results have also been validated using molecular docking simulations.

The CD spectrum of ct-DNA displays one positive peak at 275 nm due to the base pair stacking while a negative peak around 245 nm is due to the helicity. It is known that intercalating molecules affect the CD spectra of DNA while groove binders did not show any considerable influence[41] As evident from the figure. Three, that complex has some effect (though not very large as expected in case of classical intercalators and also not very small or negligible anticipated for groove binders) on the CD spectrum of ct-DNA. It is considered that the binding site of the complex is somewhere at the interfacial region of the intercalating site and groove region. To confirm our hypothesis we have performed dye displacement assays using EB which is a classical intercalator and DAPI which is known to bind at minor groove under our experimental conditions[26,27] and the results are shown in Fig. 6.

Both EB and DAPI display very low fluorescence emission, but the fluorescence intensity of both dyes increases multifold when these mixed with DNA solutions. Fig. 7A therefore, any molecule which binds at the particular site belongs to these dyes can displace the latter and eventually can decrease the fluorescence[40,42] the complex synthesized in the present study

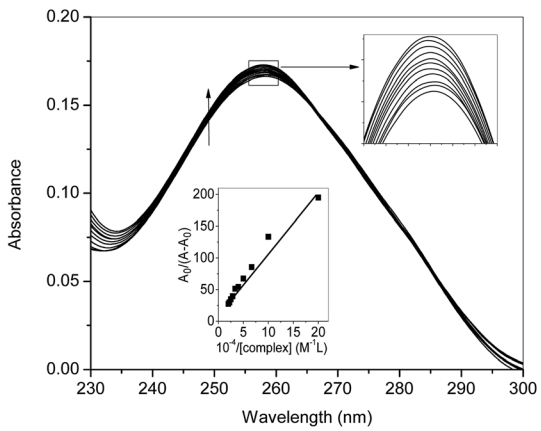

Fig. 5 Difference UV–visible absorption spectra of ct-DNA (30 μM) in the presence of increasing concentrations of nanoconjugate (0–50 μM) in Tris–HCl buffer (pH 7.4). Inset is showing the zoomed image near the wavelength of maximum absorption.

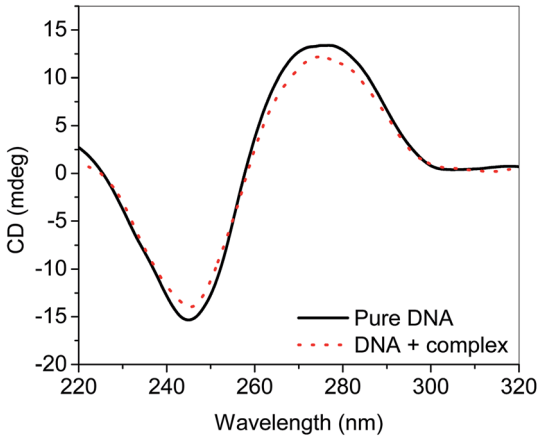

Fig. 6 Circular dichroism spectra of ct-DNA in absence and presence of complex (50 μM).

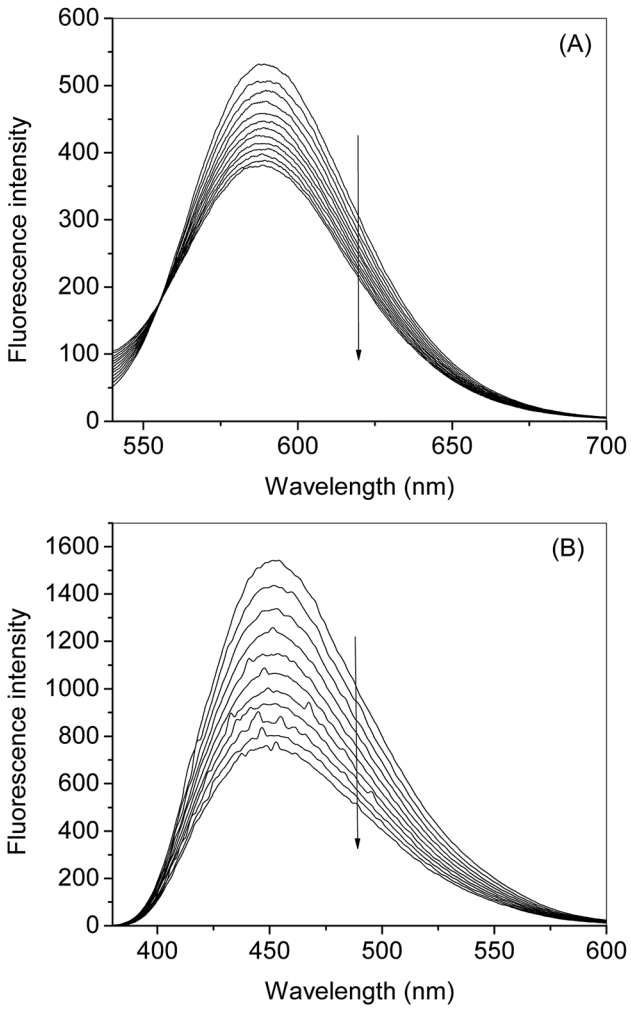

Fig. 7 (A) Fluorescence titration of EB and ct-DNA complex with nanoconjugate (0–50 μM). EB DNA complex was excited at 471 nm and emission spectra recorded from 525–700 nm. (B) Fluorescence titration of ct-DNA and DAPI (groove binder) complex with the nanoconjugate. DAPI–DNA complex was excited at 338 nm, and emission spectra recorded from 375–600 nm.

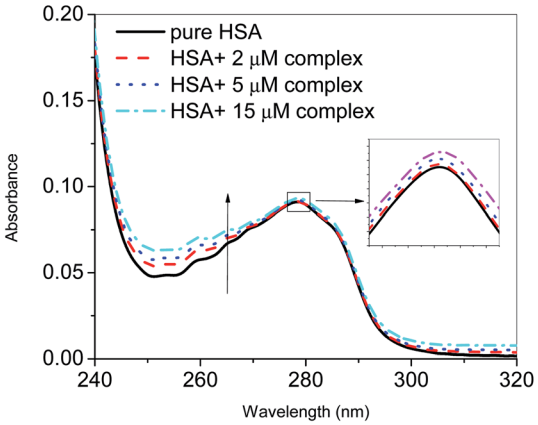

Fig. 8 UV–visible absorption spectra of HSA (2 μM) in the presence of increasing concentrations of the nanoconjugate (0, 2, 5 1 and 15 μM) in Tris–HCl buffer (pH 7.4). Inset is showing the zoomed image near the wavelength of maximum absorption.

has its own fluorescence emission at the excitation wavelength of the DAPI. However, it does not show any fluorescence enhancement in the presence of DNA. To nullify the involvement of the fluorescence of nanoconjugate in case of DAPI emission we have taken the fluorescence emission spectra of successive addition of nanoconjugate to the DNA solution and subtracted these values from the spectra containing the DAPI-DNA mixture and the subtracted spectra given in Fig. 7B. The complex did not show any fluorescence at the excitation wavelength of EB. From the dye displacement study of both EB and DAPI, it is clear that the complex was able to displace both the dyes from their respective solutions and hence can be considered as binding at the interfacial region of the groove and intercalating site. These results have been, further, supported by the computational method using molecular docking which has been given in the corresponding part of the manuscript.

The binding of the nanoconjugate seen with carrier protein human serum albumin (HSA). The UV-visible difference spectra of HSA alone and complexed with the complex given in Fig. 8 the results have shown that on the addition of complex to the HSA, the intensity of latter increases and the increment is directly proportional to the concentration of complex. After this we performed fluorescence quenching experiments by exciting the HSA at 295 nm, in which the protein shows its intrinsic fluorescence owing to the presence of a tryptophan residue.[42] Further, the complex didn't show any significant fluorescence in the region of HSA emission. However, due to the significant absorption of the complex in the region of fluorescence emission of HSA, the fluorescence data were corrected for the inner filter effect while calculating the quenching and binding parameters[43] the fluorescence quenching spectra of HSA in the presence of complex at 25, 35, and 45 °C is given in Fig. S6A–C,† respectively. The complex is capable of quenching the fluorescence of HSA efficiently which means a strong interaction between them. Stern–Volmer quenching constants have been calculated to elucidate the type of interaction using the following equation:[42]

$$F_0/F = 1 + K_{SV}[Q] \quad (2)$$

$$\log\left(\frac{F_0 - F}{F}\right) = \log K_b + n \log[Q] \quad (3)$$

$$\ln K_b = \frac{-\Delta H}{RT} + \frac{\Delta S}{R} \quad (4)$$

$$\Delta G = \Delta H - T\Delta S \quad (5)$$

where, F_0, F, $[Q]$, K_{SV}, K_b and n are the fluorescence intensity of HSA in absence of quencher, fluorescence intensity of HSA in presence of quencher, concentration of quencher, Stern–Volmer quenching constant, binding constant and number of binding sites, respectively. ΔG, ΔS and ΔH are changes in the free energy, entropy and enthalpy of interaction, respectively.

The fluorescence quenching of biomolecules by the ligands takes place either *via* a static or dynamic type of mechanism.

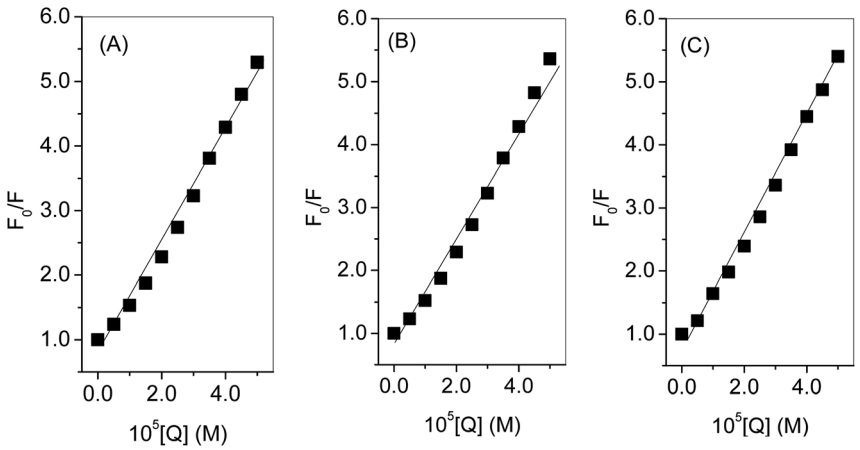

Fig. 9 Stern–Volmer plots of HSA-complex interaction at 25 °C (A), 35 °C (B) and 45 °C (C).

Table 2 Stern–Volmer quenching constants, binding parameters and thermodynamic parameters for the interaction of HSA with the nanoconjugate at various temperatures

Temperature (°C)	$10^4\ K_{sv}$ (M^{-1})	n	$10^6\ K_b$ (M^{-1})	ΔG (kJ M^{-1})	ΔH (kJ M^{-1})	ΔS (J K^{-1} M^{-1})
25	8.0	1.4	9.8	−39.9	4.4	148
35	8.1	1.4	10.7	−41.4		
45	8.3	1.4	11.0	−42.9		

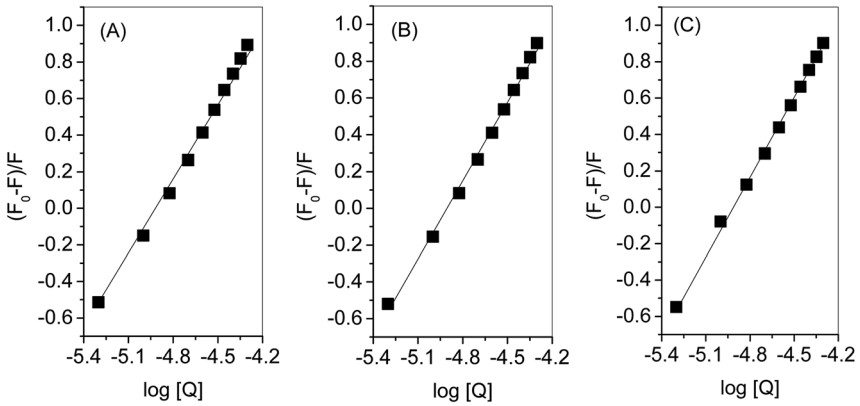

Fig. 10 Binding of HSA-complex interaction at 25 °C (A), 35 °C (B) and 45 °C (C).

Both quenchings can be differentiated by their behavior concerning the temperature.[42] Quenching constant in case of static mechanism decreases on increasing the temperature while it increases for dynamic quenching. Therefore, the fluorescence quenching measurements have been carried out at three different temperatures (25, 35 and 45°) and the values of Stern–Volmer quenching constants (analyzed according to eqn (2) using Fig. 9) given in Table 2. Increase in temperature causes a decrease of Stern–Volmer quenching constant, hence; it can be concluded that dynamic quenching is involved in the interaction between HSA and complex.

Evaluation of binding constant and number of binding sites was carried out using eqn (3) and Fig. 10 for which the values a given in Table 2. There was 1 : 1 strong binding between HSA and complex. Thermodynamic parameters were evaluated (Table 2) from the linear regression of Fig. 11 using eqn (4) and (5). A high value of ΔG is ascribed to the strong interaction between HSA and complex. From the values of ΔH and ΔS the involvement of electrostatic forces as well as hydrogen bonding is estimated in the interaction.[44]

CD was also performed to see the secondary structural changes in the protein and it was found that addition of nanoconjugate resulted in the decrease in the helicity of HSA (Fig. 12).[23,45]

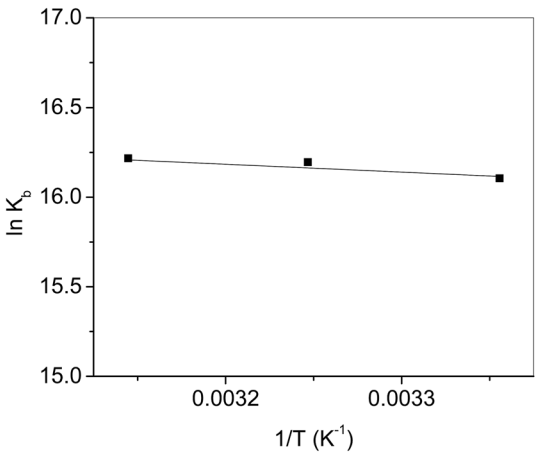

Fig. 11 Van't Hoff plots of HSA-complex interaction.

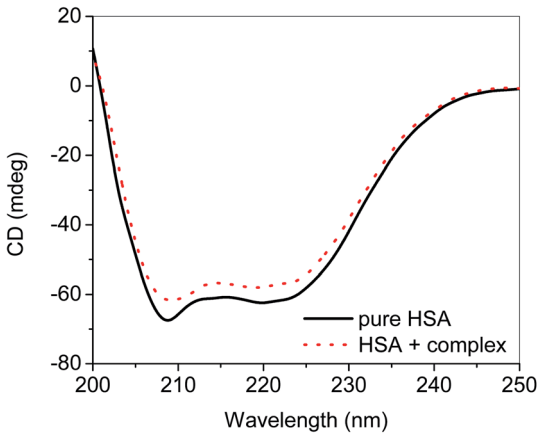

Fig. 12 Circular dichroism spectra of HSA (2 μM) in absence and presence of complex (50 μM).

3.4. pH-Dependent fluorescence studies

The fluorescence studies of the nanoconjugate were performed at different pH and observed that the conjugate has high fluorescence at pH-10 and stable (Fig. 13 and 14) at pH-4–pH-10 the intensity of the peaks increased when we move from lower to higher pH. The nano-CoO–umbelliferone has pH-dependent

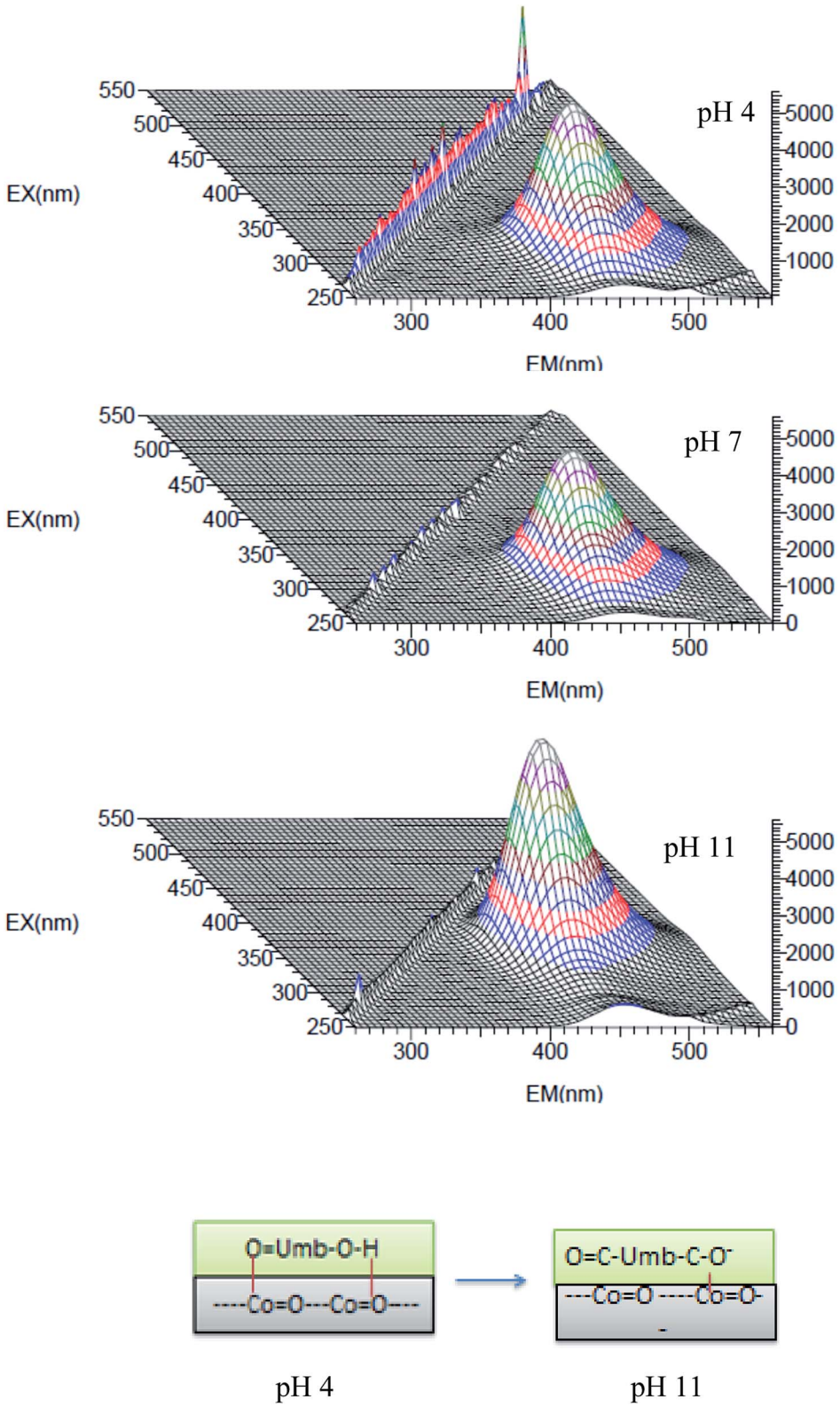

Fig. 13 Effect of pH on the 3-d spectra of nanoconjugate pH 4, pH 7 and pH 11 at 25 °C.

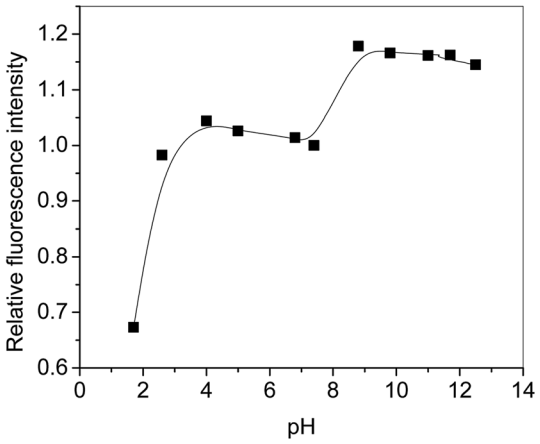

Fig. 14 Relative fluorescence intensity of complex as a function of pH at 25 °C. The fluorescence intensity at pH 7 has been taken as a standard to calculate the relative intensity.

fluorescence behavior may be considered as an active probe property for drug dispersion and action observation. The pH dependent fluorescence exciting 330–360 nm wavelength and emission peak absorbance shifted to ~450 nm, the shift is due to hydrogen bonding with nano-cobalt oxide and umbelliferone hydroxyl group (–Co═O$^{\delta-}\cdots{}^{+\delta}$H–$^{-}$O–umb–C═O) further if enhanced the intensity of the fluorescence may be due to (Co═O–umb–O^{-} + H^{+}) deprotonating in aqueous solution[46] the stability further enhanced due to electrostatic attraction within nanoconjugate.

3.5. Comparative antiproliferative studies of TiO with CoO–umbelliferone conjugate

Titanium oxide nanoparticle has been used for anti-cancer activity and drug delivery vehicle as well. Since titanium oxide has its therapeutic impact on cancer cells lines, therefore, researchers have considered it as an active delivery agent for drugs and gene vector.[47,48] The literature on cytotoxicity of TiO_2 support that TiO_2 nanoparticles have a high effect on the breast cancer cell line.[11,49–51] Some studies reported the synergistic effect of UV radiation and TiO_2 nanoparticles on several cells, nanoparticles react with a water molecule *in vitro* and yield ROS *via* electron capture pathway.

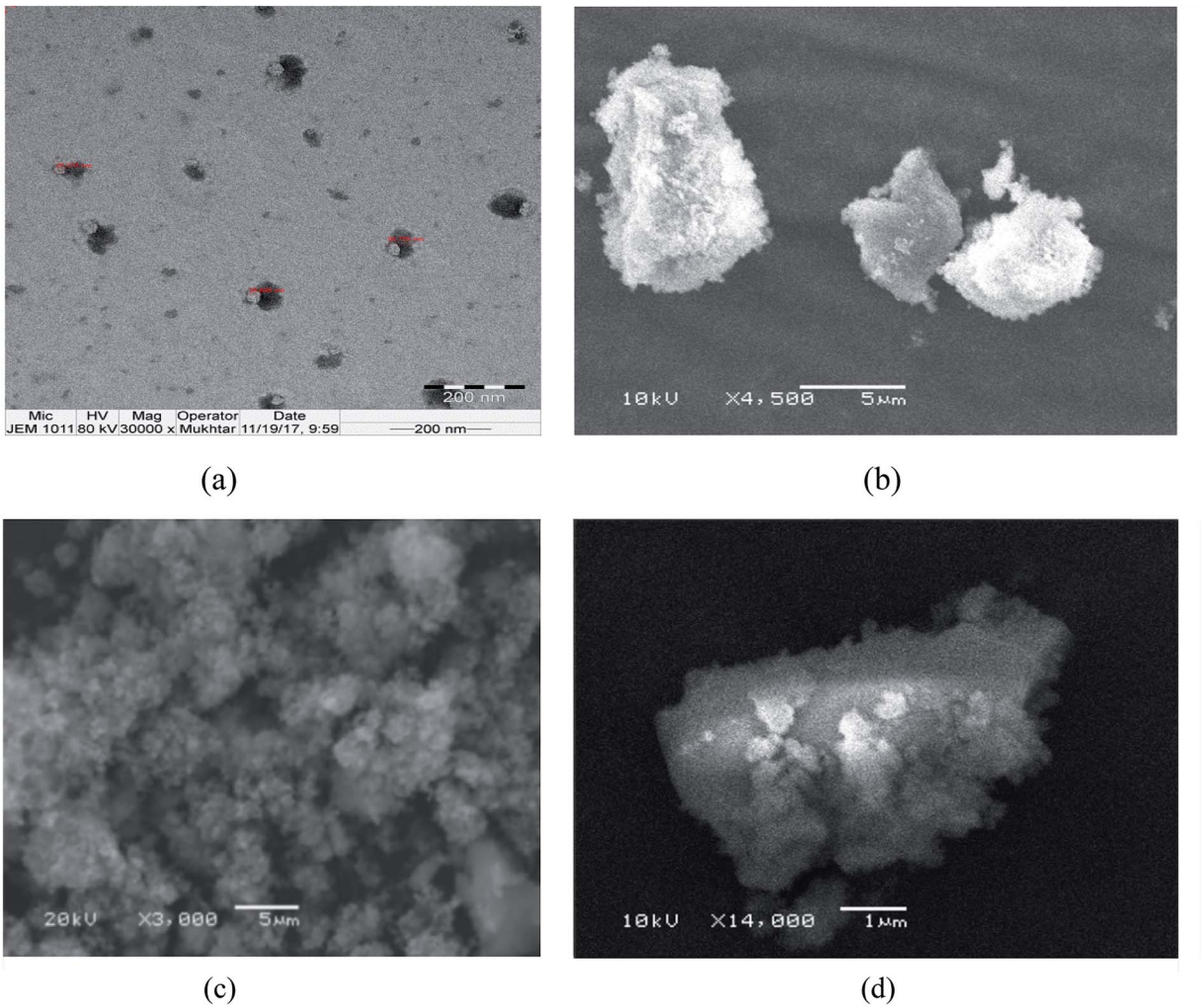

Fig. 15 TEM (a) and SEM (b–d) of nano-conjugate TiO_2 composite.

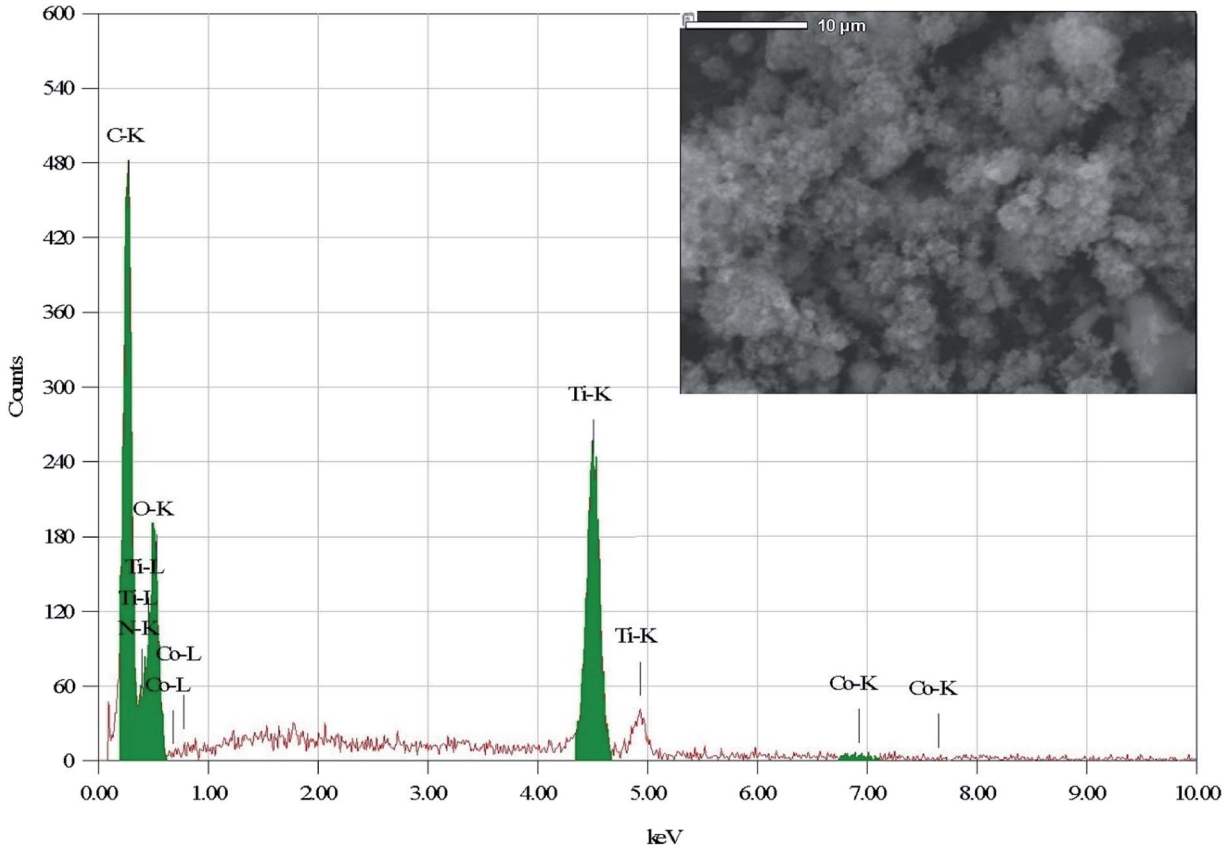

Fig. 16 EDX of the nanoconjugate-TiO_2 composite.

The titanium nanoconjugate prepared by mixing of CoO umbelliferone and TiO_2 with ultra-sonication and the dried nanoparticles analyzed by SEM and TEM, EDX analysis, the size of the mixed nanoparticles was 22–56 nm and EDX confirmed the presence of both the particles TiO_2 and umbelliferone conjugate (Fig. 15 and 16). We have compared the anticancer activity of our CoO–umbelliferone conjugate with TiO_2, and found that the proposed nanoconjugate has similar activity *in vitro* system. The IC_{50} value were compared and concluded that the CoO umbelliferone has promising activity *in vitro* anticancer evaluation.

3.5.1. Cytotoxicity. Cytotoxic activity of TiO_2, complex and Mix was evaluated by MTT assay (Fig. 17). A concentration dependent significant ($p < 0.05$) decrease in the cell viability was observed in MCF-7 cells treated with test compounds. The cell proliferation was inhibited to 65%, 69% and 73% by TiO_2, complex and Mix, respectively, at highest concentration of 250 µg mL^{-1}. The IC_{50} values estimated at 24 h post-treatment in these cells is 150 µg mL^{-1}, 130 µg mL^{-1} and 104 µg mL^{-1} for TiO_2, complex and Mix, respectively. These data suggest that Mix exhibited higher cytotoxicity in MCF-7 cells compared to the other compounds. In the subsequent experiments for autophagy, ROS, and DNA fragmentation assay, half of the IC_{50} for each test compound was applied.

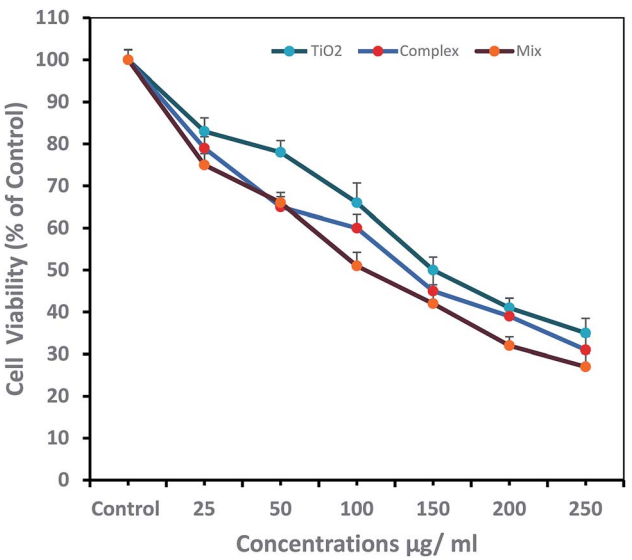

Fig. 17 Proliferation of MCF-7 cells evaluated by MTT cytotoxicity assay. The cells were exposed to indicated concentrations of TiO_2, complex and Mix respectively, for 24 h. All data are expressed as mean ± SE for three independent experiments. *Significant ($p < 0.05$) compared with corresponding controls.

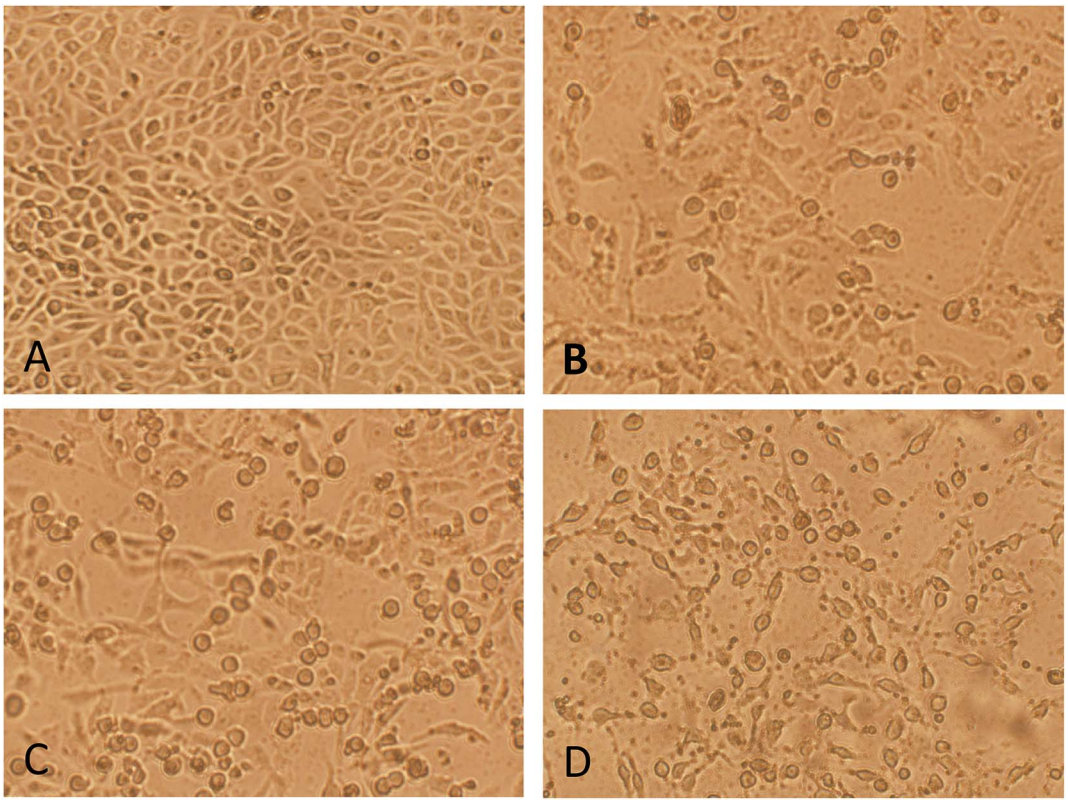

Fig. 18 Morphological analysis of MCF-7 cells observed under phase contrast inverted microscopy. The cells were exposed to half of the IC_{50} concentrations of TiO_2 (75 μg mL^{-1}, B), Complex (65 μg mL^{-1}, C) and Mix (52 μg mL^{-1}, D) and untreated control (A) respectively, for 24 h.

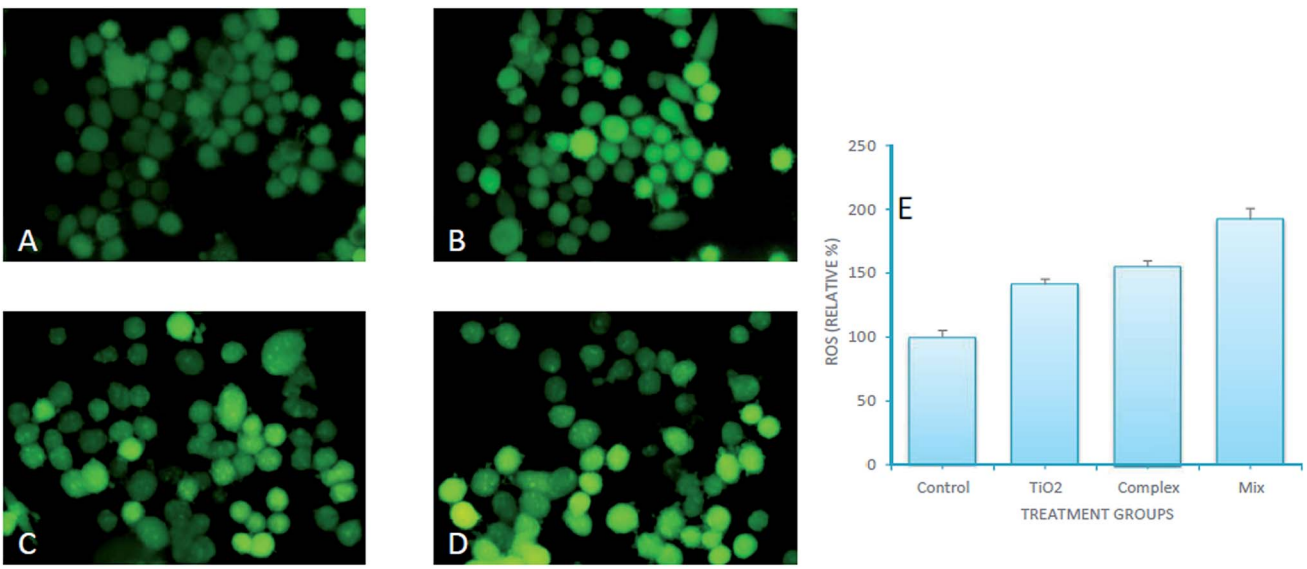

Fig. 19 Measurement of intracellular ROS by fluorescence microscopy and fluorescence intensity in MCF-7 cells. The cells were exposed to half of the IC_{50} concentrations of TiO_2 (75 μg mL^{-1}, B), complex (65 μg mL^{-1}, C) and Mix (52 μg mL^{-1}, D) and untreated control (A) respectively, for 24 h. Fluorescent intensities were measured for green fluorescence (excitation = 485 nm, emission = 530 nm) (E). The values are expressed as mean ± SE, (*Significant, $p < 0.05$).

3.5.2. Morphological changes analysis. Fig. 18A–D shows the representative images of diverse morphological alterations observed under phase contrast inverted microscopy in MCF-7 post treatment with TiO_2, complex and mix, respectively for 24 h. The morphological variations were observed such as loss of membrane integrity, cells detached from surface and becoming round, and swelled. As a result cells undergone cell death due to which cell density was decreased and many cells appeared to be floating in the medium in treated MCF-7 cells (Fig. 18B–D). Whereas control cells showed normal shape and were found attached to the surface and reached about 95–100% confluence (Fig. 18A).

3.5.3. Measurement of intracellular reactive oxygen species. To investigate the potential role of test compounds in inducing oxidative stress in MCF-7 cells, intracellular ROS generation was measured by carboxy-H_2 DCFDA assay using fluorescence microscopy and spectrofluorometry. As shown in Fig. 19B–D, after 24 hours exposure, an increase in ROS level was observed, as reflected by the enhanced green fluorescence intensity compared to the control (Fig. 19A), where only basal level of fluorescence was evident. The maximum level of intracellular ROS was seen in Mix treated cells (Fig. 19D). This pattern of intracellular ROS generation was also confirmed by quantitative estimation of fluorescent intensity, where a significant increase ($p < 0.05$) in the ROS level was recorded (Fig. 19E). When compared to the control group, an increase in 1.41, 1.55 and 1.92 fold ROS generation was recorded in TiO_2, complex and Mix treated cells, respectively.

3.5.4. Detection of autophagy by acridine orange staining. To elucidate the role of test compounds in inducing autophagy in MCF-7 cells, acridine orange (AO) was used for detection of acidic vesicular organelles (AVOs). Concentrated AO in the vesicles fluoresce bright red, whereas the cytoplasm and the nucleus show dominant green fluorescence. Staining of MCF-7 cells revealed the appearance of AVOs after treatment with TiO_2, complex and Mix for 24 hours. Fluorescence microscope images revealed control MCF-7 cells exhibited limited AVOs in the cytoplasm and showed green fluorescence with minimal red/orange fluorescence (Fig. 20A). On the other hand, the majority of treated cells exhibited more AVOs in the perinuclear region of the cytoplasm as indicator of autophagy (Fig. 20B and C).

3.5.5. DNA fragmentation. Genomic DNA fragmentation resulting in a ladder formation on agarose gel is a characteristic feature of apoptosis, and DNA laddering is a valuable technique to analyse the endonuclease cleavage products of apoptosis. In this case, treatment with TiO_2, complex and Mix resulted in DNA fragmentation and apoptosis that can be seen as a typical DNA laddering pattern (Fig. 21, lane B–D). In contrast, the control DNA exhibited a normal band of genomic DNA (lane A). The DNA fragmentation was more prominent in Mix treated MCF-7 cells (lane D).

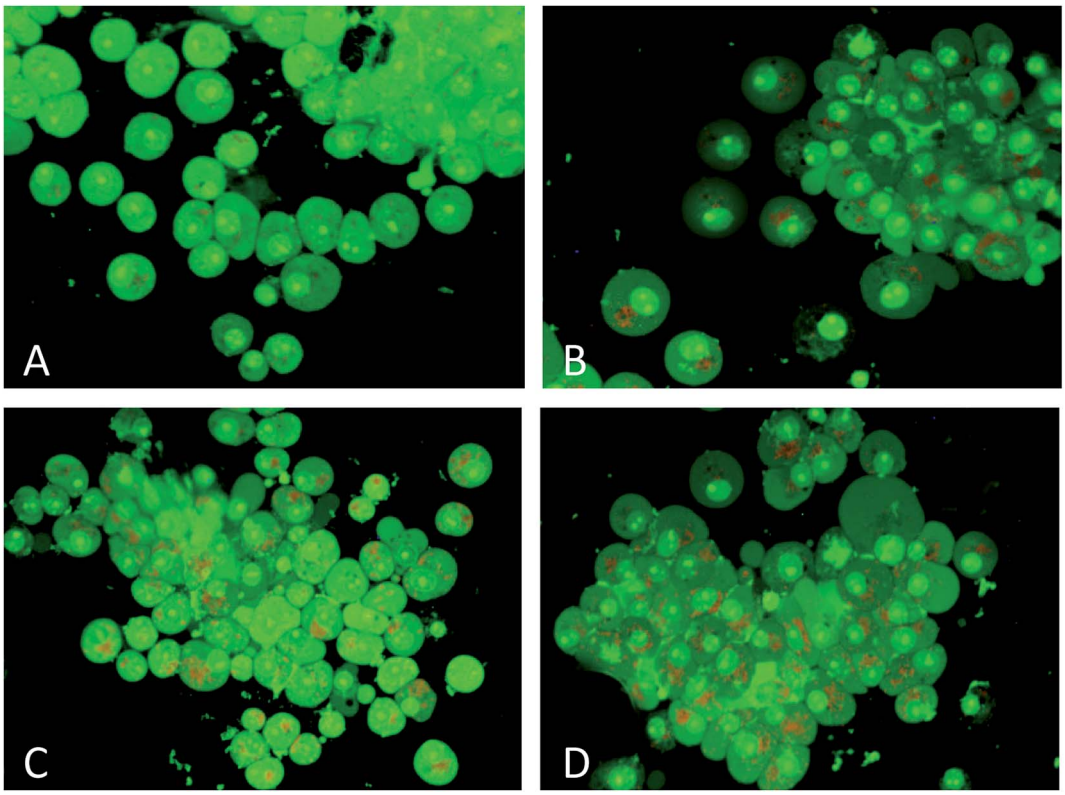

Fig. 20 Induction of autophagy was observed in MCF-7 cells through acidic vesicular organelles (AVO) staining by acridine orange. The cells were exposed to half of the IC_{50} concentrations of TiO_2 (75 μg mL^{-1}, B), complex (65 μg mL^{-1}, C) and Mix (52 μg mL^{-1}, D) and untreated control (A) respectively, for 24 h.

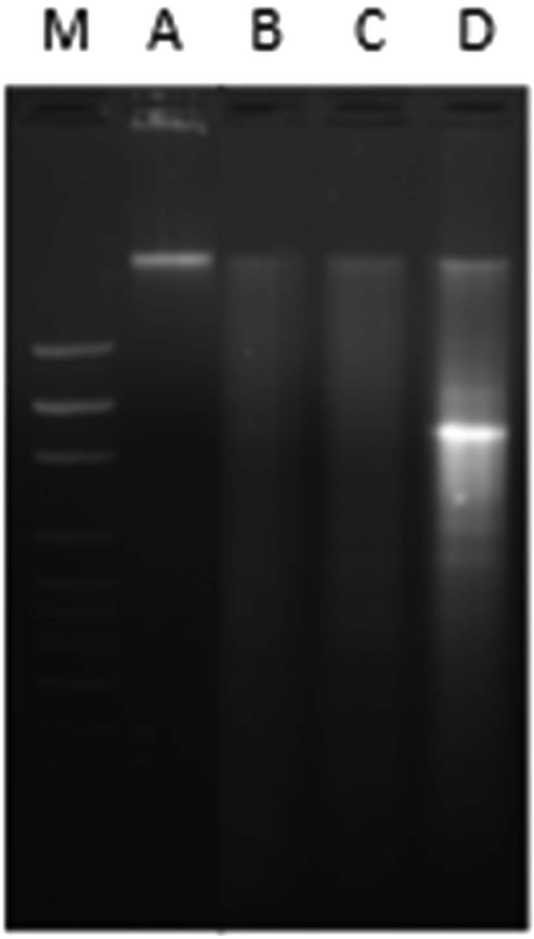

Fig. 21 DNA fragmentation analysis of MCF-7 genomic DNA by agarose gel electrophoresis. The cells were exposed to half of the IC_{50} concentrations of TiO_2 (75 μg mL^{-1}, B), nanoconjugate (65 μg mL^{-1}, C) and mix (52 μg mL^{-1}, D) and untreated control (A) respectively, for 24 h. M–100 bp DNA ladder used as molecular weight marker.

4. Conclusion

This paper deals with the new modified chemical method for the preparation of a nano-cobalt oxide conjugate of umbelliferone and study its relative influence on breast cancer cell line MCF-7 at different concentrations *in vitro*. The nano-cobalt oxide conjugate of umbelliferone has shown impressive fluorescence properties and remarkable cytotoxic potential to act as a chemotherapeutic agent as a good alternative to TiO_2. It further helps to find a better-tolerated fluorescent anti-cancer promising drug conjugate for *in vivo* studies, and seeks to ascertain the drug delivery action in the cancerous cells.

Conflicts of interest

There are no conflicts to declare.

Abbreviations

TEM	Transmission electron microscopy
EDX	Energy dispersion X-ray analysis
SEM	Scanning electron microscopy
XRD	X-ray diffraction
FTIR	Fourier-transform infra-red
ct-DNA	Calf thymus DNA
HAS	Human serum albumin
TiO_2	Titanium dioxide
JCPDS	Joint Committee on Powder Diffraction Standards
FWHM	Full width at half maximum
ESI	Electronic supplementary information

Acknowledgements

The project was supported by King Saud University, Vice Deanship of Scientific Research, Research Chair.

References

1 A. Salimi, R. Hallaj and S. Soltanian, *Biophys. Chem.*, 2007, **130**, 122–131.
2 D. S. Dimitrov and J. D. Marks, *Methods Mol. Biol.*, 2009, **525**, 1–27.
3 M. J. Dykstra and L. E. Reuss, *Biological Electron Microscopy: Theory, Techniques, and Troubleshooting*, Springer US, 2003.
4 A. M. Wu and T. Olafsen, *Cancer J.*, 2008, **14**, 191–197.
5 J. H. Rao, A. Dragulescu-Andrasi, H. Q. Yao and H. Q. Yao, *Curr. Opin. Biotechnol.*, 2007, **18**, 17–25.
6 S. M. Ansari, R. D. Bhor, K. R. Pai, D. Sen, S. Mazumder, K. Ghosh, Y. D. Kolekar and C. V. Ramana, *Appl. Surf. Sci.*, 2017, **414**, 171–187.
7 D. L. Fedlheim and C. A. Foss, *Metal Nanoparticles: Synthesis, Characterization, and Applications*, Taylor & Francis, 2001.
8 J. Lim and S. A. Majetich, *Nano Today*, 2013, **8**, 98–113.
9 E. Bermudez, J. B. Mangum, B. A. Wong, B. Asgharian, P. M. Hext, D. B. Warheit and J. I. Everitt, *Toxicol. Sci.*, 2004, **77**, 347–357.
10 A. Wiesenthal, L. Hunter, S. G. Wang, J. Wickliffe and M. Wilkerson, *Int. J. Dermatol.*, 2011, **50**, 247–254.
11 B. L'Azou, J. Jorly, D. On, E. Sellier, F. Moisan, J. Fleury-Feith, J. Cambar, P. Brochard and C. Ohayon-Courtes, *Part. Fibre Toxicol.*, 2008, **5**(1–14), 22.
12 R. B. Arora and C. N. Mathur, *Br. J. Pharmacol. Chemother.*, 1963, **20**, 29–35.
13 S. Lehnert, G. Fisher and G. Methot, *Int. J. Radiat. Biol. Relat. Stud. Phys., Chem. Med.*, 1981, **40**, 63–73.
14 N. Nizomov, A. Kholov, A. Ishchenko, V. Ishchenko and V. Khilya, *J. Appl. Spectrosc.*, 2007, **74**, 626–634.
15 M. N. Hughes, *The Inorganic Chemistry of Biological Processes*, John Wiley & Sons Incorporated, 1981.
16 S. Knutson, E. Raja, R. Bomgarden, M. Nlend, A. S. Chen, R. Kalyanasundaram and S. Desai, *PLoS One*, 2016, **11**(1–25), e0157762.
17 S. Knutson, E. Raja, R. Bomgarden, M. Nlend, A. S. Chen, R. Kalyanasundaram and S. Desai, [abstract], in *Proceedings of the 106th Annual Meeting of the American Association for*

Cancer Research; 2015 Apr 18-22, AACR; Cancer Res, Philadelphia, PA, 2015, vol. 75(15 suppl), Abstract nr LB-001.
18 S. P. Pillai, S. R. Menon, L. A. Mitscher, C. A. Pillai and D. M. Shankel, *J. Nat. Prod.*, 1999, **62**, 1358–1362.
19 Q. Zhang, J. J. Zhai, Y. R. Zhang, Y. M. Liu, L. F. Wang, S. B. Li, D. Z. Liao and G. L. Wang, *Transition Met. Chem.*, 2000, **25**, 93–98.
20 M. Usman, S. Tabassum, F. Arjmand, R. A. Khan, M. S. Ali, H. A. Al-Lohedan, A. Alsalme, M. Abul Farah, K. M. Al-Anazi and M. Ahmad, *Inorg. Chim. Acta*, 2018, **479**, 229–239.
21 D. W. Ritchie and V. Venkatraman, *Bioinformatics*, 2010, **26**, 2398–2405.
22 D. Mustard and D. W. Ritchie, *Proteins: Struct., Funct., Bioinf.*, 2005, **60**, 269–274.
23 M. S. Ali and H. A. Al-Lohedan, *J. Lumin.*, 2016, **169**, 35–42.
24 M. S. Ali and H. A. Al-Lohedan, *J. Mol. Liq.*, 2017, **236**, 232–240.
25 M. S. Ali, H. A. Al-Lohedan, A. M. Atta, A. O. Ezzat and S. A. A. Al-Hussain, *J. Mol. Liq.*, 2015, **204**, 248–254.
26 M. S. Ali, M. A. Farah, H. A. Al-Lohedan and K. M. Al-Anazi, *RSC Adv.*, 2018, **8**, 9083–9093.
27 M. S. Ali, M. A. Farah, H. A. Al-Lohedan and K. M. Al-Anazi, *J. Mol. Liq.*, 2018, **258**, 74–84.
28 K. Peters, R. E. Unger, C. J. Kirkpatrick, A. M. Gatti and E. Monari, *J. Mater. Sci.: Mater. Med.*, 2004, **15**, 321–325.
29 T. Uchino, H. Tokunaga, M. Ando and H. Utsumi, *Toxicol. in Vitro*, 2002, **16**, 629–635.
30 S. Yamaguchi, H. Kobayashi, T. Narita, K. Kanehira, S. Sonezaki, Y. Kubota, S. Terasaka and Y. Iwasaki, *Photochem. Photobiol.*, 2010, **86**, 964–971.
31 N. M. Molino and S. W. Wang, *Curr. Opin. Biotechnol.*, 2014, **28**, 75–82.
32 R. K. Sharma and R. Ghose, *J. Alloys Compd.*, 2016, **686**, 64–73.
33 B. D. Cullity, *Elements of X Ray Diffraction*, BiblioBazaar, 2011.
34 H. Esterbauer, E. Schwarzl and D. Grill, *Z. Naturforsch., C: J. Biosci.*, 1980, **35**, 682–684.
35 R. Singh, B. Singh, S. Singh, N. Kumar, S. Kumar and S. Arora, *Food Chem.*, 2010, **120**, 825–830.
36 A. Örnek, E. Bulut and M. Can, *Mater. Charact.*, 2015, **106**, 152–162.
37 T. Ahmad, *J. Nanotechnol.*, 2014, **2014**, 11.
38 G. Macindoe, L. Mavridis, V. Venkatraman, M. D. Devignes and D. W. Ritchie, *Nucleic Acids Res.*, 2010, **38**, 5.
39 B. K. Shoichet, S. L. McGovern, B. Wei and J. J. Irwin, *Curr. Opin. Chem. Biol.*, 2002, **6**, 439–446.
40 M. Sirajuddin, S. Ali and A. Badshah, *J. Photochem. Photobiol., B*, 2013, **124**, 1–19.
41 D. Sarkar, P. Das, S. Basak and N. Chattopadhyay, *J. Phys. Chem. B*, 2008, **112**, 9243–9249.
42 J. R. Lakowicz, *Principles of Fluorescence Spectroscopy*, Springer US, 2007.
43 M. S. Ali, M. Altaf and H. A. Al-Lohedan, *J. Photochem. Photobiol., B*, 2017, **173**, 108–119.
44 P. D. Ross and S. Subramanian, *Biochemistry*, 1981, **20**, 3096–3102.
45 M. S. Ali and H. A. Al-Lohedan, *Colloids Surf., B*, 2015, **134**, 392–400.
46 R. Simkovitch and D. Huppert, *J. Phys. Chem. B*, 2015, **119**, 14683–14696.
47 J. J. Wang, B. J. S. Sanderson and H. Wang, *Mutat. Res., Genet. Toxicol. Environ. Mutagen.*, 2007, **628**, 99–106.
48 S. Chattopadhyay, S. K. Dash, T. Ghosh, D. Das, P. Pramanik and S. Roy, *Cancer Nanotechnol.*, 2013, **4**, 103–116.
49 C. M. Sayes, R. Wahi, P. A. Kurian, Y. Liu, J. L. West, K. D. Ausman, D. B. Warheit and V. L. Colvin, *Toxicol. Sci.*, 2006, **92**, 174–185.
50 J. C. Lai, M. B. Lai, S. Jandhyam, V. V. Dukhande, A. Bhushan, C. K. Daniels and S. W. Leung, *Int. J. Nanomed.*, 2008, **3**, 533–545.
51 K. Peters, R. E. Unger, C. J. Kirkpatrick, A. M. Gatti and E. Monari, *J. Mater. Sci.: Mater. Med.*, 2004, **15**, 321–325.